WEP Warwick Evans Publishing

International Journal of Electric Power and Energy Studies

ISSN: 3006-2004 (Print), ISSN: 3006-0826 (Online) | Volume 4, Number 2, Year 2025
DOI: https://doi.org/10.62051/ijepes.v4n2.10
Journal homepage: https://wepub.org/index.php/IJEPES/index

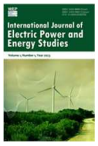

Field-scale Experiments of Oil Spill Dispersion Using Integrated UAV-LSPIV and Lightweight U-Net.

Xiao Zhang, Qin Li, Tong Chen, and Qiang Wei

School of Mechatronic Engineering, Southwest Petroleum University, Chengdu, People's Republic of China.

ABSTRACT

Obtaining quantitative relationships for oil spill spreading is crucial for emergency decision-making, but existing laboratory studies have limitations in replicating natural turbulence and acquiring field data. To address this deficiency, this study integrates unmanned aerial vehicle large-scale particle image velocimetry (UAV-LSPIV), a lightweight U-Net network, and morphological segmentation algorithms (contour accuracy of 85%) to establish a dynamic on-site monitoring system for oil spills. Lake experiments quantified three phases static diffusion (800 mL expanded rapidly to 9.72 ± 0.24 m² within 30 s, grew by +5.6 m² during 30–60 s, and stabilized near 18 m² after 70 s.), while river experiments revealed shear-driven shuttle-shaped evolution across three flow regimes (0.68–1.50 m·s-1). Small spills (200 mL) exhibit 0.001–0.005 m·s-1 faster equilibrium velocities compared to larger spills. The methodology provides a paradigm for field oil spill experiments and a field-validated dataset, which is of significant importance for improving oil spill models and emergency response.

KEYWORDS

Oil Spill Dispersion; UAV-LSPIV; Field Experiments; Deep Learning; Emergency Response.

1. INTRODUCTION

The expansion of global energy infrastructure has driven persistent annual growth in refined oil pipeline networks, where leakage incidents increasingly trigger domino effects. These accidents not only incur huge direct economic losses but also generate compounded environmental catastrophes attributable to petroleum products' high volatility and toxicity. Particularly in river-crossing pipeline segments, hydraulic forces propel rapid downstream dispersion of oil to ecologically sensitive zones, with emergency response windows typically constrained within six hours – the most critical risk scenario. Current emergency protocols critically depend on predictive modeling accuracy for oil slick trajectories, creating urgent needs for authentic field data to validate model reliability under operational conditions.

Contemporary investigations into petroleum product transport mechanisms primarily employ laboratory-scale physical modeling. Through systematic experimentation with standardized hydraulic facilities – notably the Norwegian SINTEF weathering flume, French CEDRE weathering flume, Ohmsett test basin (USA), Shanghai University's tidal-current flume system, and Harbin Institute of Technology's glass circulation flume [1-3] – researchers have established quantitative relationships between hydrodynamic parameters and oil dispersion characteristics.

This experimental paradigm extends to specialized configurations including rectangular (Kou et al., 1985; Liu et al., 2020; Jiang et al., 2021) [4-6], annular (Wu et al., 2020) [7], and polygonal flume geometries (Ulises et al., 2020) [8]. Emerging methodologies such as 3D-printed river morphologies (Cao, 2022) [9] have advanced hydrodynamic similitude have enhanced simulation fidelity. However,

Content from this work may be used under the terms of CC BY-NC 4.0 licence (https://creativecommons.org/licenses/by-nc/4.0/).
Published by Warwick Evans Publishing.

extant research faces limitations: (1) Replicating the turbulent structure and riverbed adsorption effects of natural rivers in laboratory settings is challenging; (2) Field experiments are constrained by environmental regulations, leading to a dearth of empirical data; (3) Conventional measurement techniques (e.g., buoy tracking) pose data loss risks in high-velocity flow zones. These challenges introduce inaccuracies in the practical application of existing models, significantly impeding the effectiveness of emergency response efforts.

To address these challenges, this study introduces Unmanned Aerial Vehicle (UAV) Large-Scale Particle Image Velocimetry (LSPIV) technology for real-time monitoring of river oil spills to enhance understanding of oil spill dynamics. Building upon advancements in UAV hydrological measurement technology spanning from 2015 to 2021 (Fujita et al.,15 phase analysis method; Detert et al., 2017 multi-segment splicing; Lewis et al., 2018 integration of UAV and fixed-point shooting; Cao et al., 2021 hovering flow measurement)[10-13], an experimental protocol is devised.

Subsequent dynamic observations of natural rivers are conducted to investigate the evolution of oil slicks systematically. These findings offer a more precise scientific foundation for validating oil spill models, implementing emergency response measures for oil spills, and undertaking environmental remediation efforts.

2. EXPERIMENTAL DESIGN AND SITE CHARACTERIZATION

2.1. Theoretical Framework for Experimental Design

2.1.1. Multiphase Transport Mechanisms of Riverine Oil Spills

Following an oil spill in a river, the oil undergoes multiple transport and transformation processes, including drifting, diffusion, weathering, and physicochemical interactions (**Figure 1**). The migration of spilled oil is governed by two primary mechanisms:

(1)Surface Transport: The oil slick drifts due to combined hydrodynamic (water current) and aerodynamic (wind) forces, leading to progressive thinning and expansion. Lightweight components evaporate and oxidize rapidly under environmental exposure.

(2)Subsurface Transport: Turbulence and wave action disperse portions of the slick underwater, forming oil-in-water or water-in-oil emulsions. Over time, oil clusters may coalesce, while some fractions settle onto the riverbed, where biodegradation by aquatic microbes occurs.[14,15]

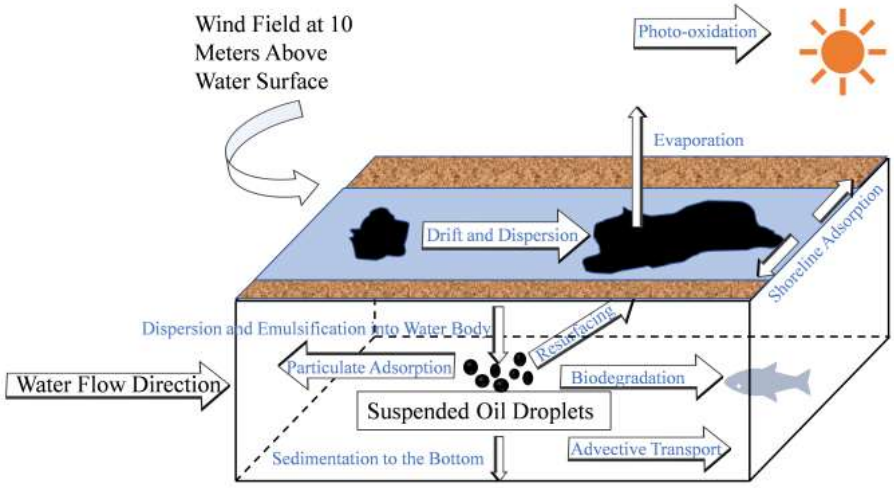

Figure 1. Behavioral fate of oil spills on rivers

Given the multi-stage migration mechanisms described above, and considering the challenges in observing underwater oil transport, as well as the predominance of surface oil films in real-world pollution scenarios, this experiment focuses on tracking the migration dynamics of river surface oil slicks.

2.1.2. Fay Extension Theory

Considering the effects of gravity, inertia, surface tension, and viscosity on the oil slick, a three-stage formula for oil slick expansion is proposed based on the various forces acting on the film during the expansion process. The formulas for calculating the diameter of oil slick expansion in each of the three stages are presented below.

Inertial force extension phase:

$$d = 2k_i(\Delta g \mathbb{V} t^2)^{1/4} \tag{1}$$

Sticky force extension phase:

$$d = 2k_v(\frac{\Delta g V^2 t^{3/2}}{v^{1/2}})^{1/6} \tag{2}$$

Surface tension expansion phase:

$$d = 2k_t(\frac{\sigma^2 t^3}{\rho_w^2 v})^{1/4} \tag{3}$$

Where d is the oil slick diameter in meters, Δ is equal to $1-\frac{\rho_o}{\rho_w}$, ρ_o is the oil phase density in kg·m^{-3}, ρ_w is the water phase density in kg/m^3, g is the gravitational acceleration in m·s^{-2}, V is the initial oil slick volume in m^3, t is the expansion time in seconds, v is the viscosity of water in m^2·s^{-1}, σ is the surface tension of air-water minus the oil-water and oil-air surfaces in N·m^{-1}, and k represents empirical constants for the three phases (1.14, 1.45, and 2.30).[16]

Building upon Fay's theoretical framework (Equations 1-3) that establishes the quantitative relationship between spill volume (V) and diffusion diameter (d), and by environmental protection considerations, this experiment was designed to investigate three distinct spill volume gradients (200 mL, 400 mL, and 800 mL).

2.1.3. Oil Spill Riverine Drift Dispersion Dominant Mechanism

Although the oil spill has multiple destinations, such as weathering, dispersion, and sedimentation in the water body, the surface drift diffusion process, as the most critical migration form of the accident, directly determines the scope of pollution, the emergency containment window, and the precision of environmental impact assessment. Given the need to prioritize the oil slick migration trajectory and diffusion rate in the actual emergency response, this experiment focuses on the water surface drift diffusion, and its core control factors are[17]:

(1)Water drag force: Driving the whole oil slick to migrate with the flow.

(2)Wind drag force: change the direction and speed of oil slick migration

(3)Oil slick diffusion by itself: diffusion perpendicular to the water flow method.

The drift velocity is deduced from the Euler-Lagrange theory as:

$$v_{drift} = a_w v_{w10} + a_c v_c \tag{4}$$

Where, v_{drift} is the oil spill water surface drift speed, $m \cdot s^{-1}$; a_w is wind drag coefficient is taken as 0.002~0.003; v_{w10} is wind speed at 10m above the water surface, $m \cdot s^{-1}$; a_c is water flow drag coefficient, generally taken as 1; v_c is water surface flow velocity, $m \cdot s^{-1}$.

According to drift velocity theory, flow velocity represents the dominant factor controlling oil slick movement. The experimental design systematically examines this relationship by testing across rivers with varying flow velocity gradients.

2.2. Site and Hydrological Characterization

(a)Field Photograph of the Experimental Lake

(b)Field Photograph of the Experimental River (Site 1)

(c) Field Photograph of the Experimental River (Site 2)

(d) Field Photograph of the Experimental River (Site 3)

Figure 2. Field Photograph of the Experimental Site

Based on the aforementioned theoretical framework and considerations of environmental sustainability and operational feasibility, this experiment selected a lake and three rivers in Guanghan City, Sichuan Province, after conducting field surveys. (Figure 2: (a)-(d)). Key features include:

(1)The experimental Lake Site is situated at Tanjiaheba, Guanghan City (104.36°E, 31.04°N), featuring a lake surface approximately 150m wide and 200-300m long, with a water depth ranging from 1.5m to 3m. Characterized by a low water exchange rate and minimal water surface fluctuation (less than 0.1m).

(2)River Site 1 is situated 500 meters east of Xigao Farm, Mayan Village, Gaoping Town, Guanghan City, at coordinates 104.16°E, 31.05°N. It spans a length of 4500 meters and has a width ranging from 5 to 7 meters, with a consistent width of 5.5 meters. The river exhibits a stable flow regime transitioning from laminar to a weak turbulent state. Throughout the river, there are 3 to 4 0.5-diameter eddies distributed randomly. The adhesion rate(measured via 1m×1m quadrat sampling) of water plants on the river banks ranges from 5% to 8%.

(3)River Site 2 is situated approximately 300m northwest of Zhangjiaguizilin (104.17°E, 31.04°N) in Mayan Village, Gaoping Town, Guanghan City. It spans 3300m in length and 4-5m in width. Owing to low geopotential, the river channel constricts, leading to accelerated flow velocity and a complex, turbulent flow state characterized by 5-6 small to medium-sized 0.5-1 diameter eddies. Additionally, the adhesion rate of water plants on the riverbank ranges from 10% to 15%.

(4)River Site 3 is situated approximately 400 meters southeast of Fuxing, Gaoping Town, Guanghan City (104.18°E, 31.03°N). It spans a length of 2400 meters and has a width ranging from 5 to 6 meters. The surface flow of the river remains stable, exhibiting minimal turbulence. Adjacent to the riverbank, there are 1-2 small 0.2-diameter eddies. The coverage of aquatic plants attached to the riverbank ranges from 5% to 8%.

2.3. Experimental Protocol Design

The entire experiment process is divided into three stages, as shown in Figure 3.

(1)Experiment preparation stage:

- Regulatory Compliance:

• Obtain institutional ethical approval

• Complete environmental impact assessment documentation

• Secure necessary permits through consultation with local authorities and community stakeholders

- Safety Protocols:

• Conduct comprehensive safety training for all personnel

• Establish emergency response procedures for potential incidents

- Equipment Setup:

• Deploy instrumentation according to experimental design specifications

- Environmental Monitoring:

• Verify stable meteorological conditions (wind speed <5 m·s-1, temperature 15-25°C, precipitation probability <10%)

• Identify a suitable 72-hour experimental window.

(2) The experiment stage includes:

- Hydrological Measurements:

• Synchronous flow velocity quantification using the buoy method and the SVR velocimeter

- Oil Spill Simulation:

• Conduct controlled releases of dyed petroleum products (200/400/800 mL volumes, 1% tracer concentration)

• Document dispersion patterns via UAV and terrestrial imaging systems

- Environmental Remediation:

• Deploy oil absorbent pad(absorbing capable:10 times its weight) for oil recovery

• Verify water quality restoration using the Portable Oil-in-Water Detector

(3) Data processing and analysis stage:

Image processing involves using software such as MATLAB, Photoshop, Agisoft Metashape, PIVlab, and others to extract data from images.

Data processing: analyze the data and conclude.

The experimental group design is shown in Table 1

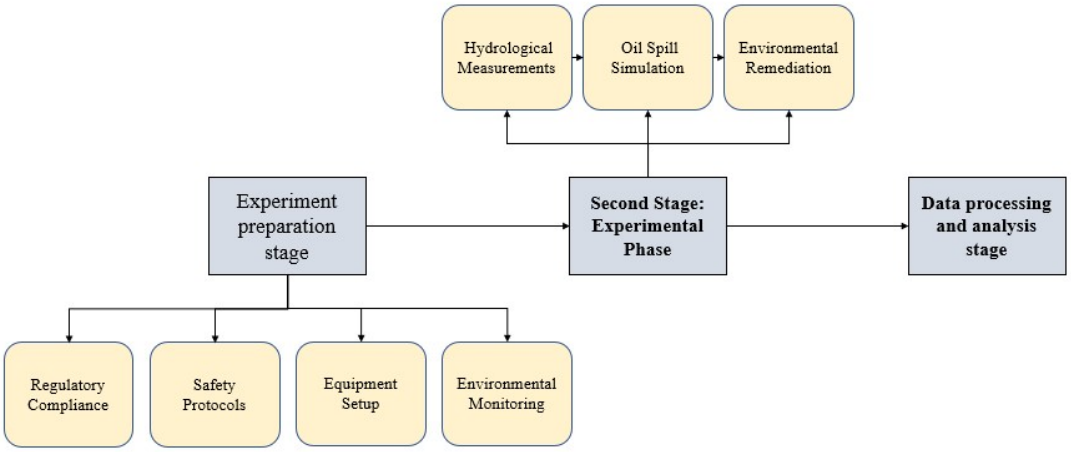

Figure 3. Flowchart of the Integrated Oil Spill Experimental Procedure

Table 1. Experimental group design matrix

Group	Location	Volume (mL)	Key Focus Parameters
G1	Lake	200	Static expansion area
G2	Lake	400	Static expansion area
G3	Lake	800	Static expansion area
G4	River Site 1	200	Leading-edge velocity and typical morphology
G5	River Site 1	400	Leading-edge velocity and typical morphology
G6	River Site 1	800	Leading-edge velocity and typical morphology
G7	River Site 2	200	Leading-edge velocity and typical morphology
G8	River Site 2	400	Leading-edge velocity and typical morphology
G9	River Site 2	800	Leading-edge velocity and typical morphology
G10	River Site 3	200	Leading-edge velocity and typical morphology
G11	River Site 3	400	Leading-edge velocity and typical morphology
G12	River Site 3	800	Leading-edge velocity and typical morphology

2.4. Experimental Methods and Equipment

2.4.1. Experimental Methods

The integrated monitoring system comprises four key components: (a) quadrotor UAV platform, (b) synchronized ground-mounted fixed camera station, (c) ground control points(GCPs), and (d) oil tracer system. As detailed in Figure 4, the UAV initiates survey transects at the upstream reach, maintaining constant altitude (10±2 m AGL) while acquiring nadir imagery of tracer dispersion patterns and riparian boundaries through systematic along-thalweg flight paths. Simultaneously, the

ground-mounted fixed camera captures images of the river surface, using GCPs for image data calibration and processing. During aerial photography, the UAV utilizes frontal or oblique imaging modes to capture images of water surface tracers. The spatial resolution of water surface images obtained through UAV frontal imaging remains consistent, effectively reducing image distortion compared to oblique photography.

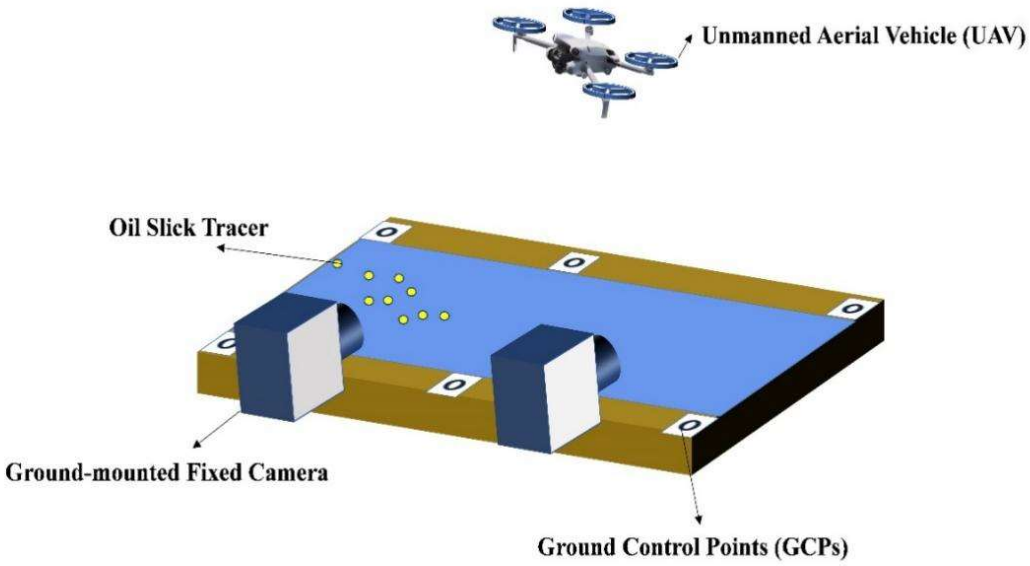

Figure 4. UAV-based measurement schematic

2.4.2. Experimental Equipment

(1)The UAV

The DJI Mini 4 Pro (SZ DJI Technology Co., Ltd.) was selected for its optimal balance between payload capacity (249 g) and compact airframe (foldable dimensions 180×90×70 mm). This micro-class UAV combines 31-minute endurance (with 3,850 mAh Li-ion battery) and 10.7 m/s wind resistance, enabling stable operation within riverine environments characterized by complex airflow patterns.

The integrated imaging payload contains a 1/1.3" CMOS sensor (f/1.7 aperture, 24 mm equivalent focal length) with dual-native ISO (100-6400) and 10-bit D-Log M color profile. Video acquisition supports 4K/100p in H.264/H.265 (4:2:0 chroma sampling), while still imagery achieves 48MP resolution through pixel-binning technology. This configuration satisfies the radiometric sensitivity requirements (SNR >42dB at ISO 800) for aqueous surface oil-film tracing applications.

(2)Biodegradable substitutes for spilled oil

Employing petroleum-derived substances in experiments presents prohibitive ecotoxicological risks (LC50 <1 $mg \cdot L^{-1}$ for aquatic organisms form GHS), mandating substitution with ecocompatible surrogates meeting standard requirements. Comparative analysis in **Table 2** reveals that edible vegetable oil demonstrates essential congruence with crude oil in key parameters:

Table 2. Comparison of Physical Properties between Crude Oil and Edible Vegetable Oil

Physical Properties	**Crude Oil**	**Edible Vegetable Oil**
Density($kg \cdot L^{-1}$)	0.8-0.95	0.91-0.93
Viscosity(mPa·s)	1-100	10-100
Solubility	insoluble in water but soluble in organic solvents	insoluble in water but soluble in organic solvents
Color	Typically dark (black, brown, etc.)	Typically light (yellow, green, etc.)

The density and viscosity ranges of crude oil are derived from API gravity classification (ASTM D1298), while vegetable oil data align with ISO 659:2009 for edible oils.

The triglyceride-based compound demonstrates superior biodegradability compared to petroleum hydrocarbons while maintaining excellent environmental stability.[18] This substitution strategy satisfies the quadripartite requirements of physicochemical fidelity, environmental sustainability, experimental reproducibility, and economic viability.

(3)Oil slick tracer

To enhance visibility and track the drift and diffusion of edible oil on river surfaces effectively, a contrasting tracer must be incorporated. This tracer should exhibit strong color contrast with the water surface, ensure environmental safety, possess optimal buoyancy, visibility, and effectively mimic the drift and diffusion patterns of the oil spill. Following a comprehensive evaluation, puffed millet, characterized by its biodegradability and ideal properties, such as a particle size of 2-3 mm and a density of 0.25 $g \cdot cm^{-3}$, was chosen as the preferred tracer for oil spill experimentation, as depicted in Figure 5.

Figure 5. Puffed millet

(4)Other auxiliary equipment

In the experiment process, it is also necessary to consider the oil spill, environmental protection, and safety, so other equipment is also needed in the experiment, as shown in Table 3.

Table 3. Other auxiliary equipment

Equipment Names	Quantity
Reference Calibration Material	Several
Flow Velocity Measurement Float	Several
Salvage Net	1
Anemometer	1
SVR Handheld Flow Velocity Meter	1
Measuring Cup	1
Life-saving Equipment	Several
Oil Absorbent Pad	Several
Portable Oil-in-Water Detector	1

3. UAV-DENOISESEG-LSPIV: AN OIL SLICK IMAGE PROCESSING FRAMEWORK INTEGRATING LIGHTWEIGHT U-NET AND MORPHOLOGICAL SEGMENTATION

3.1. System Innovation and Validation Challenges

3.1.1. Distinctive Advantages of UAV-LSPIV for Oil Slick Monitoring

UAV-based Large-Scale Particle Image Velocimetry (UAV-LSPIV) demonstrates superior performance for oil slick monitoring compared to conventional methods. Unlike fluorescence analysis (requiring laboratory processing) or buoy-based methods (susceptible to size-induced interference), UAV-LSPIV achieves real-time dynamic monitoring through high-frequency sampling (30Hz) with 0.05m spatial resolution, enabling precise capture of oil slick diffusion processes. Furthermore, this technique offers remarkable operational advantages, including low per-mission cost and flexible deployment capabilities.

3.1.2. Technical Challenges in Dynamic Water Surface Monitoring

(1) UAV hovering drift errors

During field operations, wind disturbances and manual control limitations make it challenging for UAVs to maintain a perfectly stable position. Camera pose drift due to UAV movement constitutes a primary source of measurement errors, which can be categorized as follows:

- Vertical displacement errors: Limited by the UAV's hovering control system, vertical drift remains minimal and is typically negligible.
- Horizontal displacement errors: Caused by crosswind effects at high altitudes, these induce significant lateral shifts and represent the dominant error source.
- Rotational angular errors: Yaw-axis rotation introduces uniformly distributed geometric distortions in images, which are difficult to correct using conventional methods.
- Airframe vibrations: High-frequency UAV oscillations under turbulent conditions degrade image sharpness, reducing measurement accuracy.

(2) Optical noise interference

Specular reflections from water surfaces generate overexposure artifacts that obscure oil slick boundaries, significantly compromising shape recognition accuracy. Key challenges include:

- High dynamic range interference: Reflection intensity variations exceed conventional sensor

capabilities;

- Spatially heterogeneous noise: Reflection patterns show strong angular dependence on observation geometry and solar elevation;
- Temporal variability: Wave-induced noise fluctuates rapidly ;
- Spectral aliasing: Overlapping spectra between oil slicks and reflections complicate spectral discrimination.

3.2. Core Algorithm Implementation

3.2.1. SfM-MVS-based Image Rectification

To address UAV hovering drift challenges, a multi-stage solution is implemented:

(1)Flight environment optimization:

- Selection of open areas without obstructions
- Avoidance of turbulence-prone structures (e.g., buildings, trees)
- Pre-flight anemometry to ensure wind speed <5m·s-1 (within UAV stability threshold)

(2)SfM-MVS rectification:

Structure-from-Motion (SfM) combined with Multi-View Stereo (MVS) enables:

- Camera trajectory reconstruction
- 3D scene geometry recovery
- Image sequence rectification

(Implemented via Agisoft Metashape Professional)

As a proven 3D reconstruction technique (sparse-to-dense), SfM-MVS finds wide applications in VR, autonomous driving, agriculture, etc. Figure 6 illustrates the standard UAV-based surveying workflow.

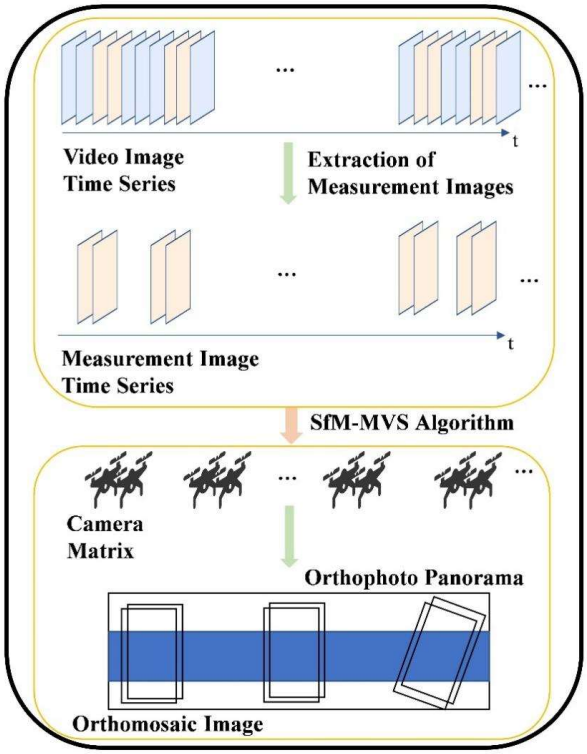

Figure 6. Image Registration Technical Flowchart

The process is as follows:

- Construction of video frame sampling strategy:

Sample the original video frame sequence matrix I_i (i = 1, 2, 3, ..., n) at intervals of s frames, extracting two consecutive frames during each sampling. Construct the measurement image sequence matrix Im_j from these extracted frames. The sampling parameters are determined by equations (1)-(3).

$$\begin{cases} \mathrm{Im}_{2k-1} = I_{(s+2)(k-1)+1} \\ \mathrm{Im}_{2k} = I_{(s+2)(k-1)+2} \end{cases} \tag{5}$$

$$k = 1,2,3,\ \cdots,\ Floor\left(\frac{n}{s+2}\right) \tag{6}$$

$$s = (1-\beta)\frac{L}{V_{drone}} f \tag{7}$$

Where: n represents the total number of frames in the original video; $Floor$ denotes the function for rounding down; β stands for the image overlap rate; L indicates the length of the coverage area in a single frame; V_{drone} is the average UAV speed; f is the frame rate for video acquisition.

- Three-dimensional coordinate transformation:

The SfM algorithm computes the projection matrix for each frame within the camera coordinate system. By integrating the ground control points' measured coordinates and the spatial coordinates of the MVS point cloud, a transformation is established from the projection matrix to the world coordinate system. This results in the conversion of the projection matrix to the absolute camera matrix in the world coordinate system. Following the monocular vision principle, a spatial point is denoted as $Q = [X, Y, Z, 1]^T$, with corresponding image plane coordinates as $q = [x, y, 1]^T$, satisfying the projection equation:

$$k_r \cdot q = P \cdot Q \tag{8}$$

where k_r is the scaling coefficient and P is a 3×4 matrix. The equation can be expanded as follows:

$$k_r \begin{bmatrix} x \\ y \\ 1 \end{bmatrix} = \begin{bmatrix} p_{11} & p_{12} & p_{13} & p_{14} \\ p_{21} & p_{22} & p_{23} & p_{24} \\ p_{31} & p_{32} & p_{33} & p_{34} \end{bmatrix} \begin{bmatrix} X \\ Y \\ Z \\ 1 \end{bmatrix} \tag{9}$$

The coefficients $[x, y]$ and P_{ij} are established values resulting from the multiplication of the camera's internal parameter matrix and external parameter matrix, while the remaining coefficients are unknown. This equation signifies the correspondence between individual pixel coordinates within the image matrix and spatial lines within the world coordinate system.

- Ortho image generation:

Utilizing the dense point cloud derived from Multi-View Stereo (MVS) within the global coordinate system enables the creation of a Digital Elevation Model (DEM) representing the water surface and river banks. By employing formula (5), the spatial straight line can be ascertained. Integration of the DEM dataset allows for the determination of the nearest point on the spatial straight line, thereby converting pixel coordinates to global coordinates. Subsequently, leveraging the elevation values associated with all pixel points and their respective RGB values, an interpolated algorithm facilitates the generation of a regional orthographic image.[19,20]

3.2.2. Lightweight U-Net-Based Oil Slick Contour Extraction

To address the non-stationary, highly dynamic specular reflection noise in non-oil slick regions, this study proposes a novel three-stage processing framework:

(1) Data-driven dynamic noise sampling

(2) Lightweight U-Net-based denoising

(3) Frequency-domain post-processing and morphological segmentation

Key technical implementations are detailed below:

(1) Data-driven dynamic noise sampling

The training dataset is enhanced through stochastic noise injection (Eq.10) combined with random horizontal flipping (Eq.11). Bicubic interpolation maintains unified resolution (edge continuity coefficient EC=0.92).

$$\begin{aligned} I_{noisy}^{(i)} &= Resize(I^{(i)}) + \lambda \cdot \mathcal{N}(0,1) \\ \lambda &= \alpha \cdot (0.8 + 0.4\eta), \quad \eta \sim U(0,1) \end{aligned} \tag{10}$$

Where: $I^{(i)} \in [0,1]^{H \times W \times 3}$ represents the original input image, λ the dynamic noise coefficient (scaling factor), α indicates the baseline noise level, η is a uniformly distributed random variable.

The data augmentation module incorporates random horizontal flipping:

$$\Phi(I) = \begin{cases} I_{noisy}^{(i)} & if\ \eta \le 0.5 \\ Flip\left(I_{noisy}^{(i)}\right) & otherwise \end{cases} \tag{11}$$

(2) Lightweight U-Net architecture[21],[22]

As illustrated in Figure 7, the network comprises:

- Encoder: Multi-level downsampling for deep feature extraction mathematically described by Eq.12.

$$E_l = MaxPool_{2\times2}\left(LReLU_{0.2}\left(BN\left(C_{3\times3}^{(64)}(E_{l-1})\right)\right)\right) \tag{12}$$

- Decoder: Spatial resolution is restored through transposed convolutional upsampling, mathematically described by Eq.13.

$$D_l = C_{3\times3}^{(128)}\left(LReLU_{0.2}\left(BN\left(TC_{2\times2}^{(128)}(D_{l-1})\right)\right)\right) \tag{13}$$

- Output layer: Standard Mean Squared Error loss:

$$\mathcal{L} = \frac{1}{N}\sum_{k=1}^{N}\left\|f_\theta(X_k) - Y_k\right\|_2^2 \tag{14}$$

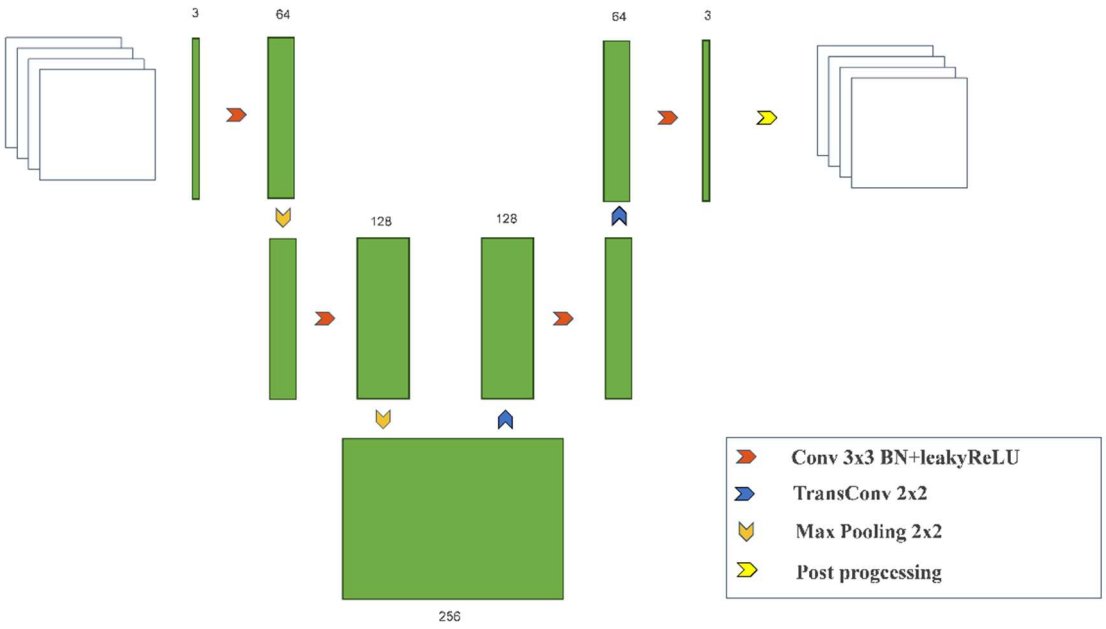

Figure 7. Lightweight U-net

Frequency-domain post-processing and morphological segmentation

Adaptive fusion: Combines Gaussian filtering with Canny-edge based weightingto balance denoising and edge preservation

Morphological processing: Fixed-threshold binarization (T=0.4) with connected-component analysis enables precise structure separation

Comparative results in Figure 8 demonstrate our method's superiority over conventional approaches (Gaussian(σ=1.5), Median(3×3), Wiener filters(5×5)). Quantitative evaluation using the matching degree metric (Eq.15) shows 85% accuracy, significantly outperforming baseline methods (~50%).

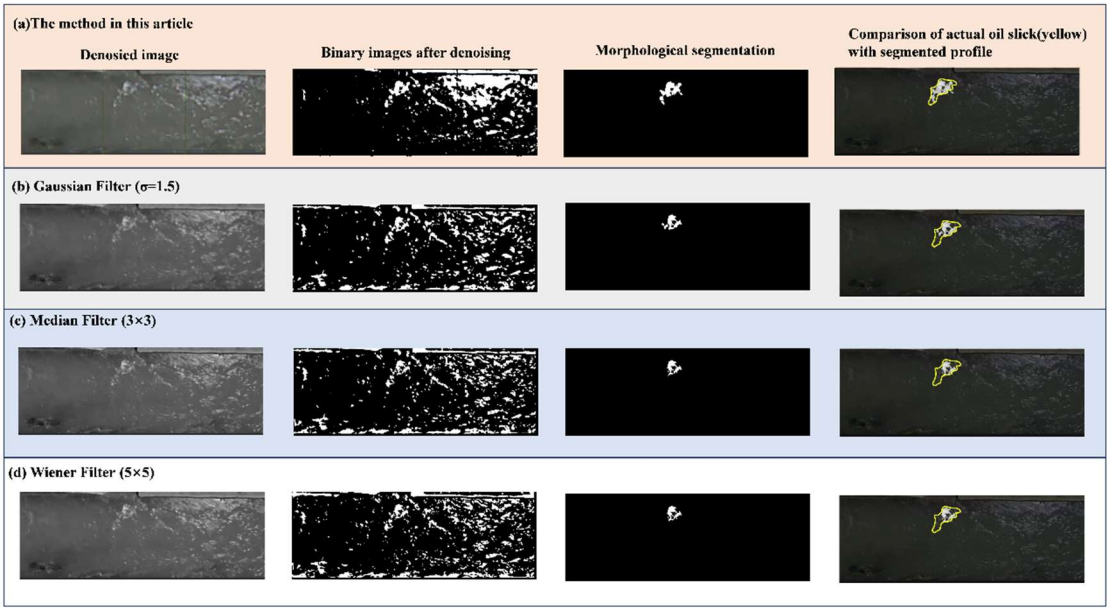

Figure 8. Comparative results between the proposed method and conventional denoising approaches

The matching degree (φ) between the detected oil slick contours and ground truth is defined as:"

$$\varphi = \frac{S_{in} - S_{out}}{S} \tag{15}$$

Where: S denotes the total number of pixels in the ground truth oil slick region, S_{in} represents the count of correctly identified pixels within the oil slick boundaries, S_{out} indicates the number of misclassified pixels outside the true contours

3.2.3. PIVlab-based Flow Field Computation

Particle Image Velocimetry (PIV) is a non-intrusive method for capturing the instantaneous velocity field of a fluid. It is extensively applied in measuring flow fields across different scales. The PIV technique involves dividing particle images from consecutive frames into uniform matrix interpretation windows. Correlation calculations are then conducted between these interpretation windows and their corresponding positions in the subsequent frame image. The displacement magnitude and direction of fluid micro-clusters within the interpretation window are determined by the distance and orientation of the position with the highest correlation coefficient about the window's center point.[23]

Firstly, the image is pre-processed after uniform size to obtain better flow field calculation by enhancing the tracer particle signal and reducing the background interference. The specific process is as follows:

(1) Convolution of the original image matrix using a 2D filter to generate the background image matrix.

(2) The original image matrix is subtracted from the background image matrix to obtain the foreground image matrix;

(3) Gray scale stretching of the foreground image to obtain the enhanced image matrix.

Then the following calculations are performed on the preprocessed image, assuming that the interpretation window of a position in 2 consecutive image frames is M×N, and the grayscale function of the corresponding window is $g_1(i,j)$ and $g_2(i,j)$, defining $(\varepsilon,\eta)\,(-M \le \varepsilon \le M,\ -N \le \eta \le N)$ as the possible displacement generated by the movement of fluid microclusters in the interpretation window, and calculating the correlation coefficients corresponding to all possible displacements through Eq. 6, and the maximum number of displacements corresponding to the maximum number of correlations, i.e., the displacement of the center of the interpretation window is The displacement corresponding to the maximum correlation number is the displacement of the center point of the reading window.

$$R(\varepsilon,\eta) = \frac{\sum_{i=-M}^{M}\sum_{j=-N}^{N} g_1(i,j)\,g_2(i+\varepsilon,j+\eta)}{\sqrt{\sum_{i=-M}^{M}\sum_{j=-N}^{N} g_1^{\,2}(i,j)\sum_{i=-M}^{M}\sum_{j=-N}^{N} g_2^{\,2}(i,j)}} \tag{16}$$

In this paper, we use the PIVLab software, whose algorithm is based on the continuous frame enhancement image matrix, and the PIV algorithm with multiple grid iterations to compute the kth-frame displacement field at the pixel scale $U_k(x,\ y,\ \Delta x,\ \Delta y)$.[24]

4. EXPERIMENTAL OBSERVATIONS OF OIL SPILL TRANSPORT

4.1. Results of the Lake Surface

4.1.1. Experimental Observation of Oil Dispersion Processes on the Lake Surface

Based on experimental observations and analysis of multiphase flow theory, the diffusion process of oil in water can be divided into two key stages, as illustrated in Figure 9.

(1) Initial Buoyancy Drive and Oil Cluster Formation Phase

The initial oil-water interaction is governed by hydrodynamic fragmentation, where impact forces generate polydisperse droplets spanning centimeter to millimeter-scale dimensions. These discrete phases undergo buoyancy-driven transport toward the air-water interface, subsequently forming continuous surface films through spreading phenomena. During the advection process, Marangoni stresses arising from viscosity gradients and interfacial tension dynamics promote droplet-droplet coalescence, leading to progressive oil mass agglomeration. The oil release height significantly impacts this process - elevated discharge positions impart greater entry velocity to the oil, enabling deeper oil column penetration and consequently extending the duration required for complete resurfacing.

(2) Oil slick diffusion and multi-level fractal fragmentation stage

After rising to form large oil aggregates, the oil slick undergoes significant multi-level fractal fragmentation. Initial rupture produces centimeter-sized oil patches, exhibiting typical fluid dynamic instability branching patterns. Subsequent size reduction leads to the formation of millimeter-sized oil droplets, during which oil-water interface interactions predominantly govern the breakup process. Prolonged exposure to wind shear transforms these discrete oil droplets into an emulsion layer, with optical opacity decreasing over time to below the visible detection threshold. This fractal fragmentation phase is extremely rapid, completing within 10 seconds ± 2 seconds.

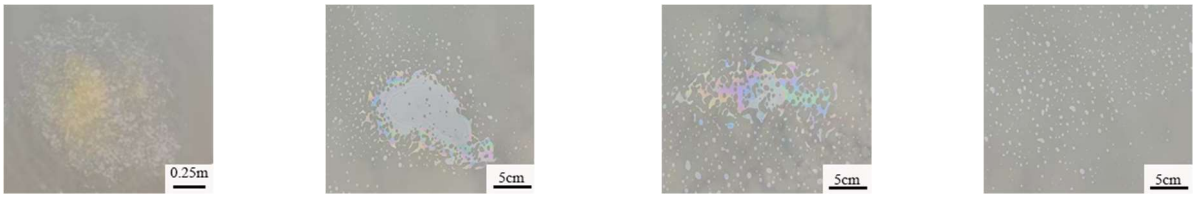

(a) buoyancy-driven oil surfacing | (b) Clustered oil slick patches (decimeter-scale) | (c) Film-like oil slick patches (centimeter-scale) | (d) Droplet-shaped oil slick spots

Figure 9. Oil dispersion processes on the lake surface

4.1.2. Results of the Oil Spill Spreading Area and Rate

The oil spill diffusion experiment was carried out on the lake surface with three different spill quantities of 200 mL, 400 mL, and 800 mL. Taking the quantity of 200 mL of oil as a representative, the original image of the oil diffusion shape and area change on the lake surface is shown in Figure 10. The oil spilled onto the lake surface started to diffuse radially in all directions. Subsequently, under the influence of the breeze, the diffusion distance along the wind direction is slightly larger than the diffusion distance perpendicular to the wind direction, and the oil slick diffusion shape slowly changes from circular to oval-like diffusion.

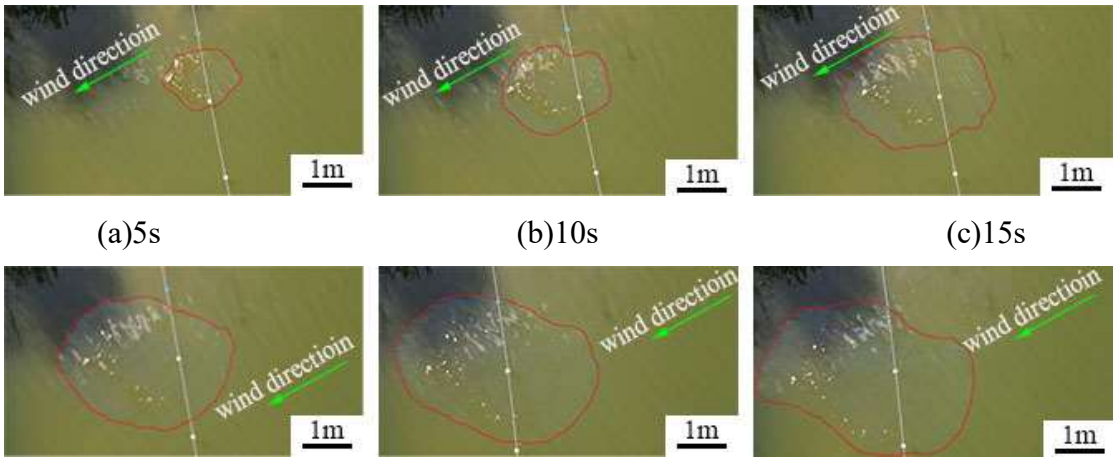

(a)5s (b)10s (c)15s

(d)20s (e)25s (f)30s

Figure 10. Diffusion process of 200 mL of spilled oil in 10- 60s

The flow field diagram obtained after PIV treatment is shown in Figure 11, and the area change and maximum diffusion velocity curves are shown in Figure 12

The experimental results demonstrate that oil slicks (200 mL, 400 mL, and 800 mL) exhibit volume-dependent nonlinear spreading dynamics across three distinct phases. During the initial rapid growth phase (0–30 s), the 800 mL slick expanded significantly faster than the 200 mL variant (9.72 ± 0.24 m^2 vs. 7.09 ± 0.14 m^2), showing volume-correlated expansion rates (800 mL: 0.125 ± 0.001 m s^{-1}; 200 mL: 0.121 ± 0.002 m s^{-1}). The subsequent transition phase (30–60 s) maintained volume-dependent area increments (800 mL: +5.60 m^2; 200 mL: +4.01 m^2), while revealing exponential decay in expansion rates (400 mL: 0.119 → 0.011 m s^{-1}). In the saturation phase (60–70 s), volume effects became statistically insignificant, demonstrated by overlapping growth rates (800 mL: 0.0109 ± 0.0003 m s^{-1}; 200 mL: 0.0098 ± 0.0010 m s^{-1}) and converging final areas (800 mL: 17.10 ± 0.28 m^2; 200 mL: 12.40 ± 0.16 m^2). Dual-axis visualization (area: left axis; rate: right axis) illustrates the regime transition from volume-driven inertial spreading ($t < 30$ s) to surface-tension-dominated

stabilization (t > 50 s), with error bars (±SD, n = 3) confirming measurement consistency and surface-tension dominance.

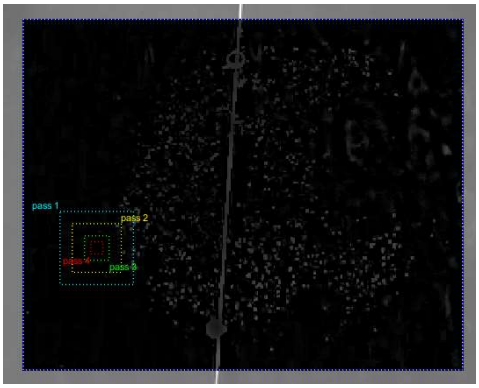

(a) PIVlab Preprocessing and Processing Window Selection

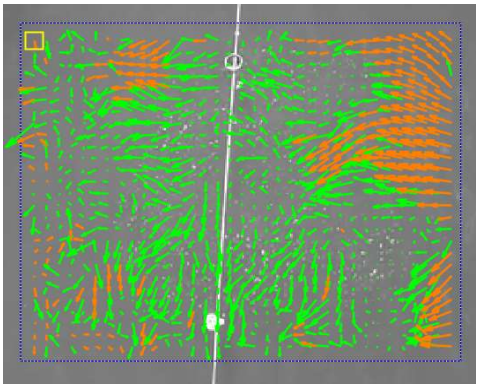

(b) PIVlab calculates instantaneous velocity vector diagrams((valid vectors (green), invalid vectors (orange))

Figure 11. PIVlab Processing

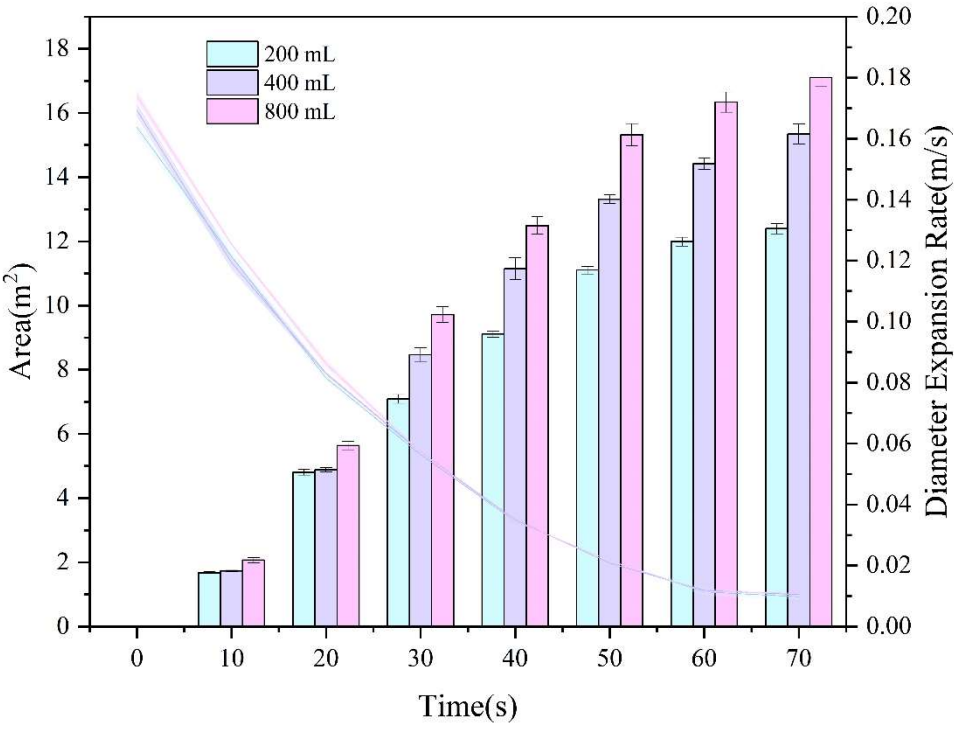

Figure 12. Relationship between Oil Slick Expansion Area (Left Y-axis, Bar Chart) and Diameter Expansion Rate (Right Y-axis, Line Graph) over Time on Lake Surface

4.2. Results of the River Surface

4.2.1. Experimental Observation of Oil Spill Dispersion Processes on River Surfaces

Through experimental observations and theoretical analysis, we systematically divide the drift-diffusion process of oil at the river surface entry into three distinct stages. **Figure 13**(a)-(c) presents these sequential phases, which illustrate the dynamic behavior of the transport mechanism.

(1) Initial Spreading Phase: Following the leakage event, crude oil spreads under the combined effects of gravitational force, inertial momentum, interfacial tension, and hydrodynamic resistance. This initiates rapid radial expansion, forming a characteristic oil slick centered at the discharge point (as shown in Figure 13(a)). During this phase, the oil slick exhibits maximum thickness with its expansion rate progressively decaying temporally. Concurrent advective transport governs the bulk movement of the petroleum mass within the aquatic system. The temporal span of this regime demonstrates parametric dependence on both the oil discharge flux and the ambient flow velocity.

(2) Shear-Driven Diffusion Phase: As the oil slick thickness diminishes below a critical threshold, hydrodynamic shear stresses supersede molecular diffusion as the primary transport mechanism. This hydrodynamic regime establishes longitudinal advection velocities exceeding lateral spreading rates by an order of magnitude, inducing morphological transition to an elongated spindle configuration (aspect ratio >3:1) as illustrated in Figure 13(b). Characteristic deceleration in areal expansion accompanies this phase, demonstrating pronounced flow-direction alignment of petroleum constituents.

(3) Quasi-Steady State Migration Phase: After full diffusion, the oil spill enters the dynamic equilibrium state. Within this regime, the oil's longitudinal transport velocity achieves congruence with the bulk river surface velocity, while interfacial turbulence fluctuations induce irregular distribution patterns documented in Figure 13(c). In open hydraulic systems, other effects such as evaporation begin to dominate the oil slick mass loss, with interfacial stability subject to coupled perturbations from multiphase transport dynamics and atmospheric boundary layer interactions.

(4) Complex hydrodynamic interactions at the air-water interface induce mechanical disintegration of the oil phase during initial water contact. This bifurcation event initiates through spatiotemporal velocity gradients and vortex shedding phenomena, generating dual distinct structures that undergo parallel advection-diffusion processes as shown in Figure 13(d). Subsequent downstream transport reveals shear-mediated morphological differentiation, where each cluster develops elongated spindle geometries through microscale shear gradients. Notably, this bifurcated evolution recapitulates the evolutionary trajectory observed in individual spill scenarios.

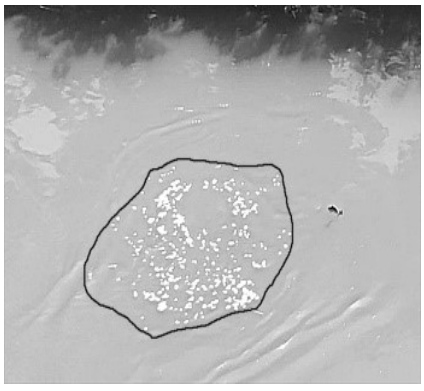

(a)Initial Spreading Phase

(b)Shear-Driven Diffusion Phase

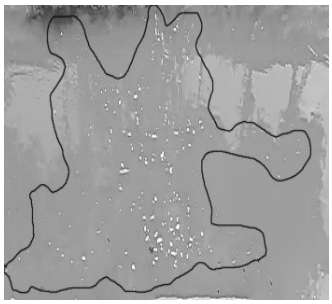

(c)Quasi-Steady State Migration Phase

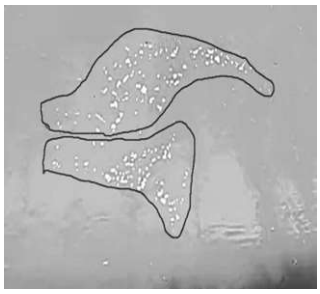

(d)Fragmentation and Concurrent Diffusion Processes

Figure 13. Typical Morphological Characteristics of Oil Slick Patches at various Phases of Drift Dispersion of Oil Spill on the river surface.

4.2.2. Measured Length and Width of Typical Oil Slick Patches

The video exported images captured by the drone and the camera were aligned and pre-processed to obtain the shape of the front end of the oil slick reaching each ground calibration point, the maximum width along the direction of the water flow and perpendicular to the direction of the water flow was measured. Experiments were conducted several times, retaining the typical diffusion shapes (rounded, shuttle-shaped, irregular sheet) experiment group, to obtain the shape of the main film (not counting the length of the bank retention) of the different leakage volume of the oil slick data under different rivers. As shown in Figure 14.

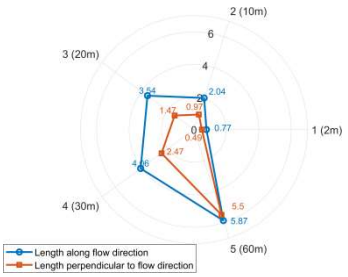

(a) 200mL oil in River Site 1

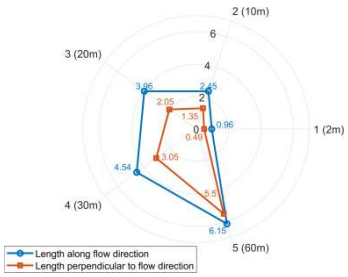

(b) 400mL oil in River Site 1

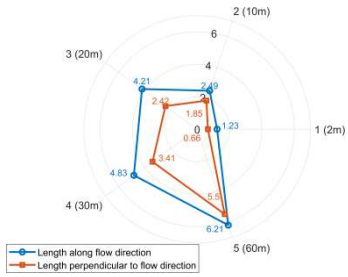

(c) 800mL oil in River Site 1

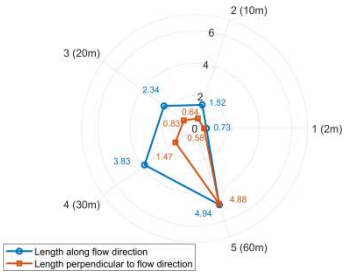

(d) 200mL oil in River Site 2

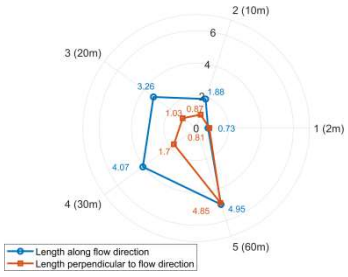

(e) 400mL oil in River Site 2

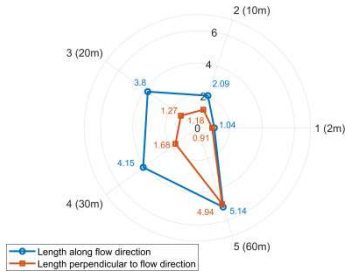

(f) 800mL oil in River Site 2

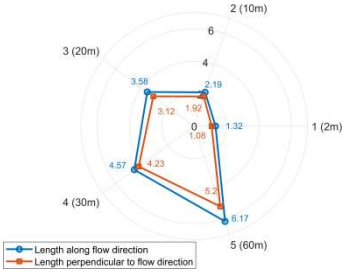

(g) 200mL oil in River Site 3

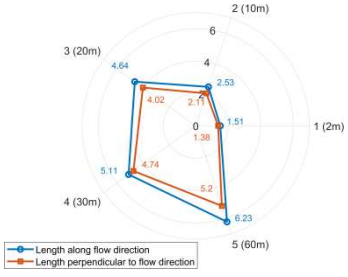

(h) 400mL oil in River Site 3

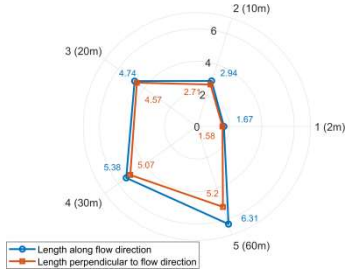

(i) 800mL oil in River Site 3

Figure 14. Measured length and width distributions of typical oil slick patches

Experimental results demonstrated flow velocity-dependent anisotropy evolution in oil slick diffusion. Increasing flow velocity from 0.7 $m \cdot s^{-1}$ (River Site 3) to 1.5 $m \cdot s^{-1}$ (River Site 2) enhanced the aspect ratio ($R = L_{flow}/L_{\perp flow}$) of 400 mL oil slicks from 1.15 to 3.17 at the 20 m GCPs downstream (Δ+202%), confirming shear-driven longitudinal stretching. However, this anisotropy diminished at the 60 m GCPs (R = 1.02), likely due to turbulence-induced isotropic mixing. Meanwhile, spill volume exhibited both temporal and marginal decay effects decay effects: 600 mL increments (200→800 mL) caused 22% (10 m) versus 5.7% (60 m) longitudinal growth at River Site 1, Marginal decay is demonstrated by the declining growth rates from 39.4% (200→400 mL at the 10 m GCPs) to 18% (400→800 mL at the same location).

4.2.3. Results of the Oil Spill Drift Spreading Rate on the River Surface

(1) River flow experiment results

The flow velocities at the center of the three streams were measured several times under windless conditions by the buoy method and SVR flow meter, and the range of mean flow velocities at the center of the three streams is shown in Table 4.

Table 4. Average Flow Velocity Range at the Surface Center Position

River	Average Flow Velocity Range at the Surface Center Position ($m \cdot s^{-1}$)
1	1.12-1.15
2	1.47-1.50
3	0.68-0.71

(2) Experimental Findings on Drift and Diffusion Rates of Oil Spills on River Surfaces

The images extracted from drone and camera footage undergo registration, pre-processing, and subsequent analysis using PIVlab software. Following multiple experiments, experiment groups containing significant abnormal data are eliminated. The velocities of the leading edge of the oil slick under varying leakage rates across different rivers are depicted in Figure 15.

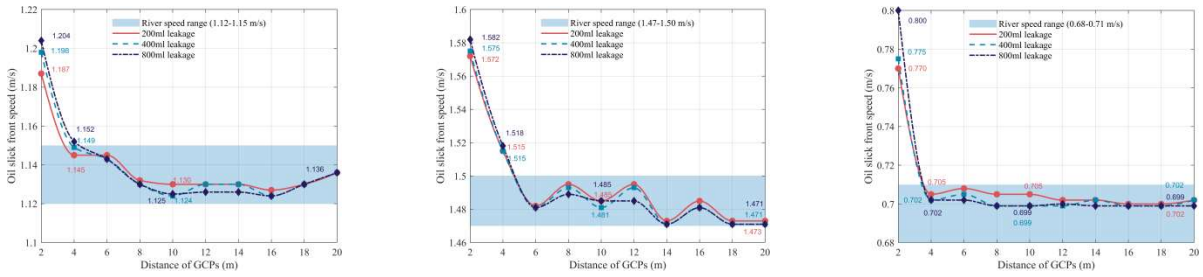

(a) River Site 1 (b) River Site 2 (c) River Site 3

Figure 15. Leading edge velocities of oil slicks with different leakage amounts in different rivers

Experimental data show that across three river velocity conditions, the diffusion velocities of the spilled oil slick exhibit nonlinear attenuation. The attenuation rate decreases as the monitoring distance increases, eventually aligning with the corresponding river velocity range and reaching a dynamic equilibrium stage. The specifics are as follows:

(1)Low flow velocity group (0.68 - 0.71 $m \cdot s^{-1}$)

The diffusion velocity rapidly decays in the initial stage (2 - 4 m) ($\Delta \approx 0.075$ m·s^{-1}). After 4 m, it overlaps with the range of river flow velocity, and the subsequent (4 - 20 m) fluctuation amplitude drops to ±0.003 m·s^{-1}. This phenomenon indicates that the flow state on the river surface is stable in the laminar-dominated environment, and the viscous shear effect is uniform, which promotes the system to quickly enter a low-disturbance equilibrium state.

(2) Medium flow velocity group (1.12 - 1.15 m·s^{-1})

The diffusion velocity decays significantly within the range of 2 - 6 m ($\Delta \approx 0.05$ m·s^{-1}), and then (6 - 20 m) stabilizes within the range of the river flow velocity, with the fluctuation amplitude maintained at ±0.006 m·s^{-1}. Compared with the low-velocity group, the fluctuation amplitude in the equilibrium state increases slightly.

(3)High flow velocity group (1.47 - 1.50 m·s^{-1})

The peak initial attenuation rate is observed between 2 to 6 m ($\Delta \approx 0.09$ m·s^{-1}), with fluctuations of ±.015 m·s^{-1} persisting from 6 to 20 m. These fluctuations may be linked to vortex separation effects caused by the turbulent boundary layer on the river surface. The sporadic transfer of turbulent kinetic energy induces local flow-velocity disturbances, which continuously influence the oil slick's spreading path.

(4)Differences in dynamic equilibrium thresholds

There are significant differences in the distance thresholds for each group to enter the dynamic equilibrium stage. Theoretical analysis shows that this threshold is jointly determined by the competition mechanism between the observation time scale ($\tau_{obs} = L/u_{river}$) and the diffusion time scale of the oil slick itself (τ_{diff}): when $\tau_{obs} \geq \tau_{diff}$, the system enters a stable state; otherwise, it maintains a transitional state.

(5)Phased impacts of the leakage amount

The influence of leakage volume on diffusion behavior shows a stage-by-stage regulation: In the initial diffusion stage (<6 m), the leakage volume is positively correlated with the diffusion speed, which may be related to the inertia-dominated mechanism in Fay's spreading theory. After entering the equilibrium stage, the diffusion speed of small leakage volumes is generally 0.001 - 0.005 m·s^{-1} faster than that of large leakage volumes, possibly because the limited kinetic energy of water flow drives the momentum transfer of small-mass oil slick with higher efficiency.

5. CONCLUSION

This study systematically investigates oil spill dispersion dynamics in rivers through UAV-LSPIV technology and field experiments, providing novel monitoring methods and empirical data for emergency response. Key findings include:

(1) UAV-LSPIV Monitoring Framework

Developed an oil slick contour extraction algorithm combining lightweight U-Net denoising and morphological segmentation (85% matching accuracy), effectively addressing specular reflection interference. SfM-MVS image rectification mitigated UAV hovering drift errors.

(2) Dispersion Regime Characterization

The experimental results revealed fundamentally different dispersion mechanisms between static and flowing water conditions. Lentic systems exhibited triphasic expansion beginning with rapid inertial expansion (800mL,0-30 s, +9.72±0.24 m²), transitioning to viscous-dominated growth rate decay (30-60 s, +5.60 m²), and finally approaching surface-tension stabilization (60-70 s, final area 17.10±0.28 m²). In contrast, lotic systems produced dynamic evolution patterns where initial gravity-inertia driven radial expansion progressively transformed into shear-dominated longitudinal stretching

(achieving aspect ratios up to 3.17:1 at 1.5 $m \cdot s^{-1}$ flow velocity), ultimately stabilizing into quasi-steady migration with velocity fluctuations (± 0.015 $m \cdot s^{-1}$) that closely matched the underlying river flow characteristics. These distinct behavioral patterns provide critical benchmarks for modeling oil spill dispersion in different aquatic environments.

(3) Operational Applications

These findings advance oil spill modeling by providing validated dynamic datasets and a low-cost monitoring paradigm, significantly enhancing preparedness for cross-river pipeline emergencies. Future work will extend this framework to chemical spills and estuarine environments with tidal influences.

The established framework contributes to predictive oil transport modeling through benchmarked hydrodynamic datasets and cost-effective surveillance protocols, which may improve operational readiness for riverine infrastructure emergencies. Subsequent research directions will adapt the proposed monitoring framework to investigate multiphase contaminant transport dynamics, particularly in tidally forced estuarine systems requiring coupled hydrodynamic-atmospheric modeling.

ACKONWLEDGMENT

The authors would like to acknowledge the funding supported by the National Natural Science Foundation of China (Nos.51974272).

CREDIT AUTHORSHIP CONTRIBUTION STATEMENT

Xiao Zhang:Experiment ,Writing - Original Draft, Resources, Software, Data analysis, Revision. Qin Li: Experiment, Methodology, Revision,Funding acquisition. Tong Chen: Experiment, Record, Data analysis. Qiang We: Experiment, Record.

DISCLOSURE STATEMENT

No potential conflict of interest was reported by the author(s).

DATA AVAILABILITY STATEMENT

The data that support the findings of this study are available from the corresponding author, [Xiao Zhang], upon reasonable request.

REFERENCES

[1] U. Bronner, O. Johansen, and F. Leirvik, Spreading of waxy oils on calm water, Mar. Pollut. Bull. 129 (2018), pp. 135–141.

[2] M. Cao, Experimental study and numerical simulation of instantaneous oil spill dispersion in northern rivers, M.S. thesis, Harbin Institute of Technology, 2011.

[3] X. Wu, B. Qiao, and Y.F. Zou, Latest research progress of oil weathering simulation test devices: A global review, Ship Ocean Eng. 47 (2018), pp. 9–14. (in Chinese)

[4] Y.Z. Kou, S. Yamazaki, and Y.L. Si, Diffusion of continuous oil spills at sea, Environ. Prot. Transp. 1985 (2), pp. 18–23. (in Chinese)

[5] D. Liu, W.Q. Lin, and B.C. Zhong, Experimental study on oil spreading and drifting characteristics in tidal rivers, J. Hydrodyn. 2006 (6), pp. 744–751. (in Chinese).

[6] P. Jiang, S. Tong, and Y. Wang, Modelling the oil spill transport in inland waterways based on experimental study, Environ. Pollut. 284 (2021), pp. 117473.

[7] S. Wang, S. Xu, and Y.F. Yang, Retention behavior of spilled crude oil along riverbanks, J. China Univ. Pet. 44 (2020), pp. 144–150. (in Chinese)

[8] U. Rojas-Alva, J. Fritt-Rasmussen, and G. Jomaas, Experimental study of thickening effectiveness of two herders for in-situ burning of crude oils on water, Cold Reg. Sci. Technol. 175 (2020), pp. 103083.

[9] Q. Cao, Study on oil drifting patterns in rivers after pipeline leakage, M.S. thesis, China University of Petroleum (Beijing), 2024.

[10] Fujita I, Notoya Y, Shimono M. Development of UAV-based river surface velocity measurement by stiv based on high-accurate image stabilization techniques.IAHR world Congress,The Hague,2015

[11] M. Detert, E.D. Johnson, and V. Weitbrecht, Proof-of-concept for low-cost and non-contact synoptic airborne river flow measurements, Int. J. Remote Sens. 38 (2017), pp. 2780–2807.

[12] Q.W. Lewis, E.M. Lindroth, and B.L. Rhoads, Integrating unmanned aerial systems and LSPIV for rapid, cost-effective stream gauging, J. Hydrol. 560 (2018), pp. 230–246.

[13] L. Cao, V. Weitbrecht, and Volker, Airborne feature matching velocimetry for surface flow measurements in rivers, J. Hydraul. Res. 59 (2021), pp. 637–650.

[14] M.E. Birpınar, G.F. Talu, and B. Gönençgil, Environmental effects of maritime traffic on the İstanbul Strait, Environ. Monit. Assess. 152 (2009), pp. 13–23..

[15] A.D. Venosa and X. Zhu, Biodegradation of crude oil contaminating marine shorelines and freshwater wetlands, Spill Sci. Technol. Bull. 8 (2003), pp. 163–178.

[16] J.A. Fay, Physical processes in the spread of oil on a water surface, Int. Oil Spill Conf. Proc. 1971 (1), pp. 463–467.

[17] Y.C. Weng, J.X. Yang, and Y.W. Jiang, Numerical simulation of drift trajectories in the Taiwan Strait, J. Xiamen Univ. Nat. Sci. 48 (2009), pp. 446–449. (in Chinese).

[18] Forero-Hernandez,Hector, and Jones, Comprehensive development, uncertainty and sensitivity analysis of a model for the hydrolysis of rapeseed oil. Comput. Chem. Eng. 133 (2020), pp. 106631.

[19] Y.C. Zhang, Z.C. Zhuang, and Y.Z. Xiao, 3D distribution of NDVI for rapeseed based on structure from motion algorithm, Trans. Chinese Soc. Agric. Eng. 31 (2015), pp. 207–214. (in Chinese)

[20] L.K. Cao, D. Martin, and D.X. Li, UAV-based surface flow field measurement system for long river reaches and its application, J. Tsinghua Univ. Sci. Technol. 62 (2022), pp. 1922–1929. (in Chinese)

[21] Olaf Ronneberger, Philipp Fischer, and Thomas Brox. U-Net: Convolutional Networks for Biomedical Image Segmentation. Medical Image Computing and Computer-Assisted Intervention – MICCAI 2015,2015,Vol.9351: 234-241.

[22] H. Zunair and A. Ben Hamza, Sharp U-Net: Depthwise convolutional network for biomedical image segmentation, Comput. Biol. Med. 136 (2021), pp. 104699.

[23] Q.G. Chen, Investigation of turbulent vortex structures in open channels using high-frequency PIV, Ph.D. diss., Tsinghua University, 2016.

[24] W. Thielicke and E.J. Stamhuis, PIVlab – Towards user-friendly, affordable and accurate digital particle image velocimetry in MATLAB, J. Open Res. Softw. 2 (2014), pp.e30.